Near Surface Geophysics   **EAGE** EUROPEAN ASSOCIATION OF GEOSCIENTISTS & ENGINEERS

ORIGINAL ARTICLE

Case study of combined marine- and land-based passive seismic surveying in front of Nordenskiöldbreen outlet glacier, Adolfbukta, Svalbard

Helene Meling Stemland[1,2] ⓘ | **Bent Ole Ruud**[1,2] ⓘ | **Tor Arne Johansen**[1,2,3] ⓘ

[1]Department of Earth Science, University of Bergen, Bergen, Norway

[2]ARCEx, UiT The Arctic University of Norway, Tromsø, Norway

[3]Arctic geology department, The University Center in Svalbard (UNIS), Longyearbyen, Norway

Correspondence
Helene Meling Stemland, Department of Earth Science, University of Bergen, PO Box 7803, 5020 Bergen, Norway.
Email: helene.stemland@uib.no

Abstract

Glaciers generate seismic waves due to calving and fracturing, meaning that recording and following event classification can be used to monitor glacier dynamics. Our aim with this study is to analyse seismic data acquired at the seabed and on land in front of Nordenskiöldbreen on Svalbard during 8 days in October 2020. The survey included 27 ocean bottom nodes, each equipped with 3 geophones and a hydrophone, and 101 land-based geophones. The resulting data contain numerous seismic P-, S- and Scholte wave events throughout the study period, as well as non-seismic gravity waves. The recording quality strongly depends on receiver type and location, especially for the latter wave types. Our results demonstrate that hydrophones at the seabed are advantageous to record gravity waves, and that Scholte waves are only recorded close to the glacier. The Scholte waves are used to estimate the near-surface S-wave profile of the seabed sediments, and the gravity wave amplitudes are converted to wave heights at the surface. We further discuss possible source mechanisms for the recorded events and present evidence that waves from earthquakes, calving and brittle fracturing of the glacier and icebergs are all represented in the data. The interpretation is based on frequency content, duration, seismic velocities and onset (emergent/impulsive) and is supported by source localization, which we show is challenging for this dataset. In conclusion, our study demonstrates the potential of using seismic observations for detecting glacier-related events and provides valuable knowledge about the importance of survey geometry, particularly the advantages of including seabed receivers in the vicinity of the glacier.

KEYWORDS
data acquisition, seismic, waves

INTRODUCTION

Glaciers are large, slow-moving bodies of dense ice undergoing various deformation processes that generate seismic signals, often referred to as icequakes (Podolskiy & Walter, 2016). In this context, seismic waves are generated due to friction between the glacier and the underlying ground (e.g., Hudson et al., 2020; Podolskiy et al., 2021), the generation of fractures and crevasses within or at the surface of the glacier (e.g., Deichmann et al., 2000; Neave & Savage, 1970), or calving at the glacier terminus (e.g., Köhler et al., 2019; Qamar, 1988). These waves then travel through the ice itself and the surrounding air, ground and water.

Seismic receivers record ground vibrations (geophones) or transient pressure changes in water (hydrophones) and can therefore be used to record seismic signals generated by the glacier. The type of wave, amplitude, duration, polarization, origin location and occurrence frequencies can provide information about the glacier dynamics, which is valuable in a climate change context as glaciers are sensitive to warming and contribute significantly to eustatic sea level rise (Meier et al., 2007; Meredith et al., 2019). Additionally, signals from the glacier can potentially be exploited as a seismic source to unveil the mechanical properties of the near-surface sediments in the vicinity of the glacier (Hudson et al., 2020). The use of such natural seismic sources is particularly advantageous in vulnerable Arctic environments where the use of active seismic sources is challenging due to logistical and environmental reasons (Stemland et al., 2019; Trupp et al., 2009).

Previous studies have shown that calving events have a different seismic characteristic to fracturing, crevassing or basal stick–slip motion, both regarding frequency content and duration (e.g., O'Neel et al., 2007; Qamar, 1988). Further, the characteristics of the calving seismic signal depend on whether the ice falls onto ground, ice or water and the calving style of the glacier. Calving of small (metre to 10s of metre-scale) ice blocks at Arctic tidewater glaciers (Bartholomaus et al., 2012; Köhler et al., 2019) causes different seismic signals than the so-called glacial earthquakes caused by calving, breakup and capsizing of larger (kilometre-scale) icebergs at the Antarctica and Greenland ice sheets (Sergeant et al., 2019; Winberry et al., 2020). Calving into water is occasionally followed by 'mini-tsunamis', which in reality are non-seismic gravity waves (Minowa et al., 2019).

Bartholomaus et al. (2012) compared visual observations of the marine-terminating Yahtse glacier terminus in Alaska with simultaneously recorded seismograms to correlate source mechanisms with recorded icequakes. They found that typical calving signals have emergent onsets, dominant frequencies between 1 Hz and 3 Hz, durations of 5–30 s and lack clear P- or S-arrivals. Similarly, O'Neel et al. (2007) associated direct observations of calving events at the marine-terminating Columbia glacier in Alaska with emergent seismic signals with dominant frequencies of 1–3 Hz, and Köhler et al. (2015) observed icequakes at frequencies of 1–8 Hz in relation to calving events using the regional seismic network in Svalbard. As opposed to calving signals, Neave and Savage (1970) first reported that seismic signals from near-surface crevassing had impulsive onsets, durations of 0.1–1.0 s and characteristic frequencies of around 100 Hz. Some decades later, Deichmann et al. (2000) showed that icequakes may also be produced at greater depths within the glacier due to brittle fracturing, and that these deep icequakes typically have higher dominant frequencies than their shallow counterparts due

to the lack of Rayleigh surface waves. In the literature, near-surface crevassing is typically reported to occur more frequently than deeper icequakes, and dominant frequency ranges are 1–5 Hz for calving events and 10–50 Hz for near-surface crevassing events (Podolskiy & Walter, 2016). Over the entire range of cryoseismic sources, signals with frequencies on the order of 10^{-3}–10^3 Hz have been recorded (Glowacki, et al., 2016; Podolskiy & Walter, 2016).

Seismic signals from Arctic tidewater glaciers have been extensively studied in the last two decades, but previous studies have mostly relied on a very limited number of receivers. In this study, we describe the details of a seismic field campaign conducted on Svalbard in October 2020. The objectives of this paper are to review the acquired seismic data for optimal survey design and to analyse the data with particular focus on the classification of various events. The novelty of our case study is the use of a total of 27 functioning ocean bottom nodes (OBN), each equipped with 1 hydrophone and 3 geophones, in combination with 101 planted land geophones to measure the seismic signals generated by a mixed-terminus tidewater glacier. In particular, we are not aware of any previous studies where such a large number of hydrophones were deployed at the seabed in front of a glacier, which we show is favourable in detecting seismic signals and non-seismic gravity waves with a high signal-to-noise ratio (SNR). We finally briefly discuss what the data reveal about the dynamics of Nordenskiöldbreen and the near-surface geology of Adolfbukta.

STUDY AREA AND DATA ACQUISITION

The study site where we placed out seismic receivers is in and around Adolfbukta (78°38′40″ N and 16°55′00″ E) in the inner part of Billefjorden on Svalbard, around 13 km east of the abandoned mining village of Pyramiden (Figure 1a,b). Adolfbukta is located in front of Nordenskiöldbreen, an outlet glacier of the Lomonosovfonna ice cap with an estimated thickness of up to 600 m, but thinning towards the terminus (Van Pelt et al., 2012). Nordenskiöldbreen is a mixed-terminus (i.e., partly terrestrial-, partly tidewater-terminating) glacier, and the marine-based (southern) margin (Figure 1c,d) has historically had more active calving and extensive crevassing than the cold-based (northern) terrestrial margin (Figure 1e,f) (Allaart et al., 2018). The glacier is polythermal and fast-flowing (up to 30–60 m/a; Den Ouden et al., 2010), with no signs of current surge activity (Ewertowski et al., 2016). However, aerial images indicate that the glacier has exhibited surge-type activity in the past (Allaart et al., 2018; Farnsworth et al., 2016). Studies of a time-series of aerial images from the area by Allaart et al. (2018) indicate 2350–3550 m glacier
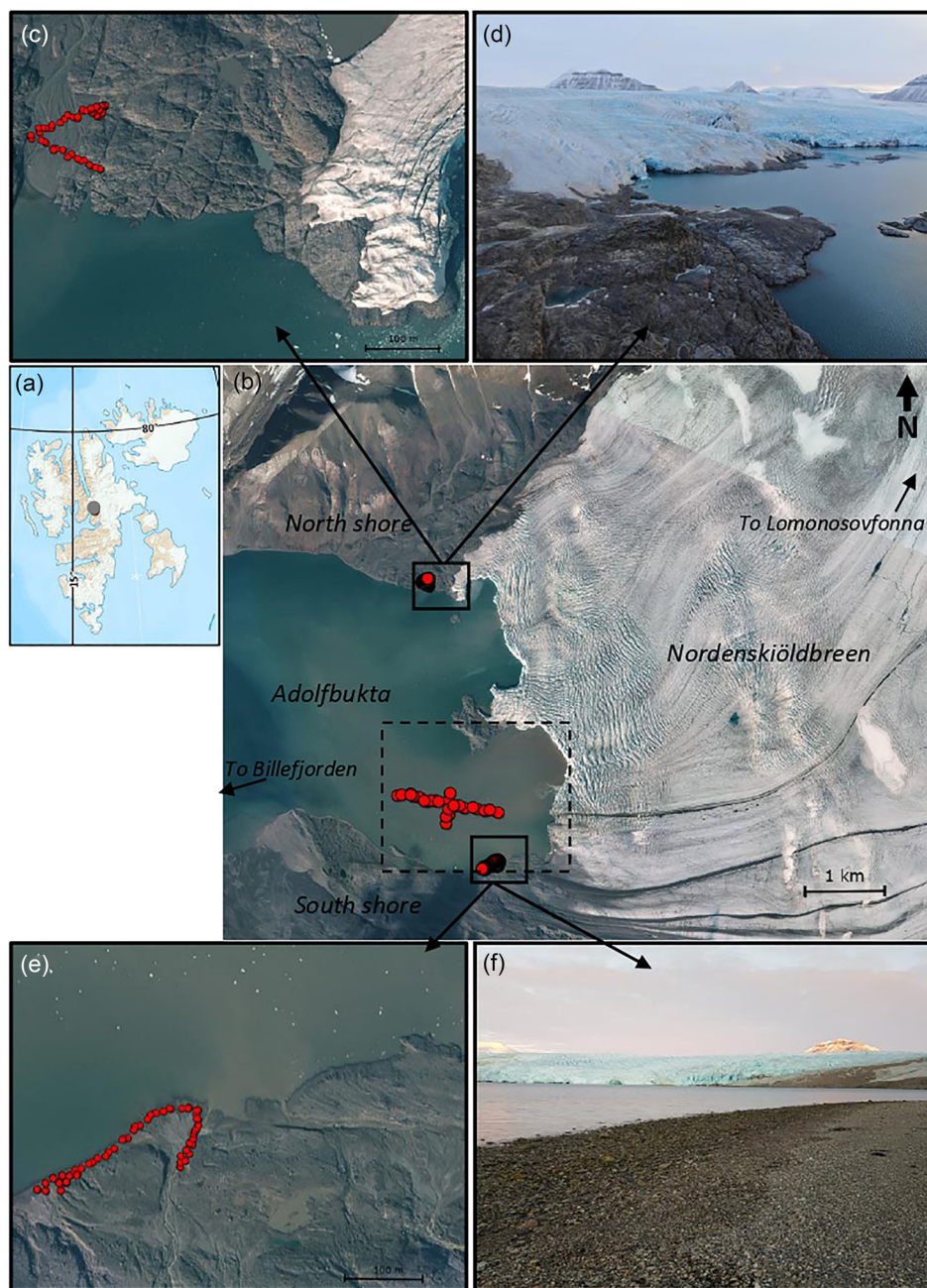
FIGURE 1 (a) The study site is in Adolfbukta in the inner part of Billefjorden (grey dot). (b) Seismic receivers (red dots) were placed out at the seabed in Adolfbukta (details from the area within the dashed box are found in Figure 2), on the northern shore and on the southern shore. Nordenskiöldbreen flows from Lomonosovfonna located northeast of Adolfbukta (outside the map) and down towards the bay, mainly in a west/southwest direction. The northern margin of the glacier is land-based, and the southern margin is marine-terminating. (c) Close-up of the North array (d) view towards the glacier from the North array, (e) close-up of the South array (f) view towards the glacier from the South array. The layouts of the land lines were mainly determined by ground conditions. *Source*: Maps/satellite images courtesy of Norwegian Polar Institute (toposvalbard.npolar.no)/Copernicus Sentinel data.

retreat during the years 1896–2015, and the current retreating trend of most glaciers in Svalbard suggests further retreat subsequently.

The reflection seismic study of Blinova et al. (2013) in combination with numerous geological studies of Svalbard (see, e.g., Elvevold et al., 2007) indicate that

the subsurface in Billefjorden consists of metamorphic basement rocks, overlaid by a thick layer of low-reflective Devonian sandstones. Above these are thinner layers of evaporites and carbonates from the Carbaniferous and Permian, characterized by strong, parallel and continuous seismic reflections. Due to subsequent strong uplift
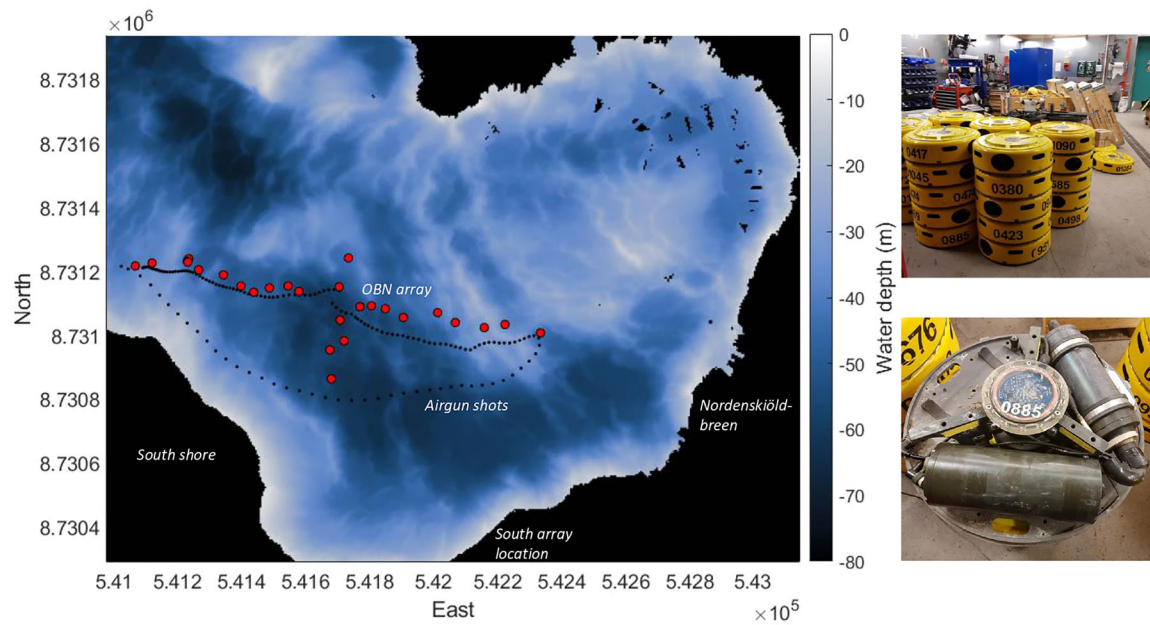
FIGURE 2 A total of 27 ocean bottom nodes (OBNs) (red dots) were recording at the seabed in the southern part of Adolfbukta. Black dots are airgun shots. The area in the figure corresponds to the dashed box in Figure 1. Previously acquired bathymetry data show that the water depth over the OBNs varies between 30 and 60 m. The black area is unmapped area/land. The pictures show the OBNs used. *Source*: Bathymetry data acquired by the Norwegian Hydrographic Survey (2009) and UNIS (2014) (see Allaart et al., 2018). The scientific colour map 'Oslo' is retrieved from Crameri (2018).

and erosion, consolidated layers above these have been eroded in inner Billefjorden, and they are directly overlaid by unconsolidated glaciogenic deposits from the Quaternary. Plassen et al. (2004) reported that the maximum thickness of the unconsolidated sediments is 65 m proximal of the terminal moraine in Adolfbukta. Elsewise, little is known about the seismic properties of the near-surface sediments in the area.

We deployed 40 OBNs (Seabed Geosolutions, Trilobit) at the seabed in Adolfbukta, out of which 27 were successfully recovered with complete data at the end of the acquisition period (11–18 October 2020) (Figure 2). Each OBN had a hydrophone (High Tech, Inc. HTI-96-Min, low-cut frequency of 3.6 Hz with a filter slope of 6 dB/octave) and a three-component geophone (Sensor SM-6, 14 Hz, Galperin configuration). In addition, a total of 20 (10 + 10) planted 3C geophones, and 81 (45 + 36) vertical component spike four-geophone strings were placed out on the southern and northern shore of the bay, respectively. All land-based geophones had a natural frequency of 10 Hz and a spurious frequency of 240 Hz.

The large number and variety of receivers included in the experiment is a novel part of this study, and there are several reasons why increasing the receiver number is advantageous. First, the various receiver types may record different types of waves and are differently affected by background noise. Figure 3 shows one event recorded by (a) the OBN hydrophones, (b) the

OBN geophones and (c) the strings of vertical geophones at the south array. The event is visible in all records, and the comparison of the amplitude spectra reveals similar dominant frequencies for all receivers. However, the background noise in the OBN geophones overlaps with the dominant frequencies of the glacier signals, and the land geophone signal quality strongly depends on ground coupling and weather conditions. In particular, we observed decreased land node data quality further out in the study period, probably because temperature variations, wind and water waves flooding the array reduced the geophones' ground coupling and increased their tilt throughout the week. Furthermore, data recorded on soft sand at the south shore (like those in Figure 3c) are of higher quality than those from the north shore where the ground was rocky and with pebbles. Hence, we use data from the OBN hydrophones to classify events as these have the overall lowest noise level during the study period, but also use the land geophone data for discussing the localization of events.

Second, both geophones and hydrophones record P-waves independently of their location, but hydrophones only record S-waves when they are converted to P-waves (e.g., at the seabed interface). On land, Rayleigh surface waves can be recorded on vertical component geophones, and Love waves can be recorded on horizontal component geophones, whereas in water, Scholte waves are mainly best recorded on geophones
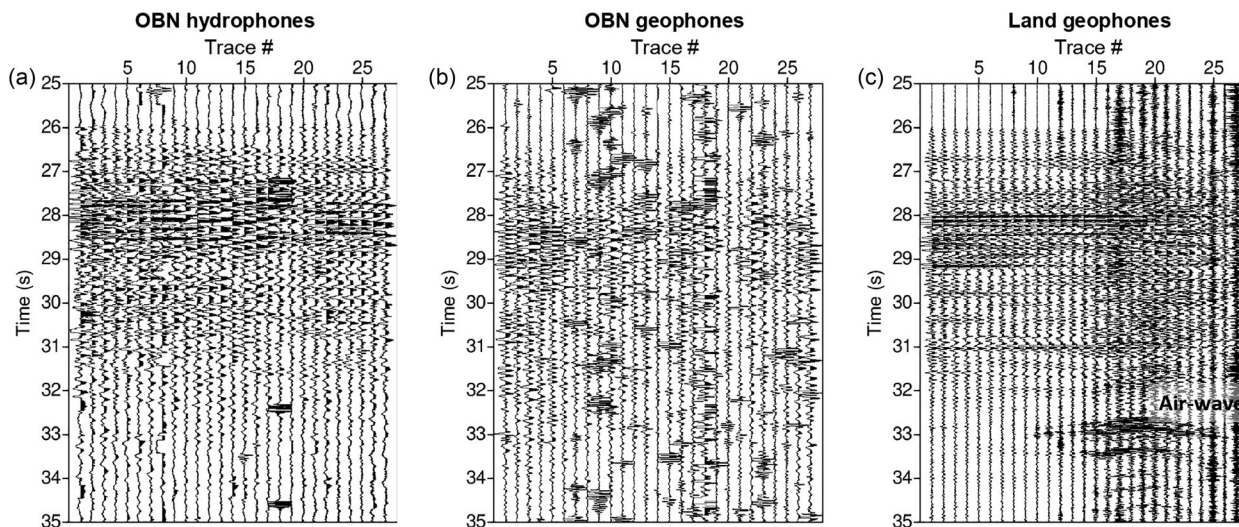
FIGURE 3 The event on October 11 at 1400 UTC recorded on (a) ocean bottom node (OBN) hydrophones, (b) OBN geophones and (c) south array vertical geophone strings. The event consists of several overlapping phases arriving between approximately 26 and 32 s. Background noise affects all data gathered but is more dominant on geophones. OBN traces are ordered from east to west, that is from closest to the glacier to most distant from the glacier, and bandpass-filtered from 1 to 150 Hz. In the latter figure, the event starting at 32.7 s is an air wave. Note that the data recorded furthest away from the shore (i.e. the first 15 traces in (c)) were more sheltered from wind and water waves and are thus of the best quality, whereas traces 16–27 are much more affected by noise.

or hydrophones located close to the seabed (Johansen & Ruud, 2020). Third, increasing the number of receivers can make it easier to localize the source of the seismic wave and further help to determine the source mechanisms. As discussed later in this paper, the complex source function of calving signals still makes source localization a challenge here.

The seismic receivers that were placed out in and around Adolfbukta were passively recording the entire study period, and these data recordings are mainly analysed below. Additionally, on 14 October, 141 seismic shots were fired using an airgun located at 3 m water depth. The airgun shots were used to determine the coordinate positions, including the depth, of the OBNs, as well as calibrating the directivity of the 3C geophone components. We also use the seabed reflections evident in zero offset hydrophone data to estimate the water depths in the area to be 30–60 m (assuming a water velocity of 1460 m/s), which is consistent with the bathymetry data in Figure 2. The OBN recordings of the airgun shots further reveal refracted waves travelling with an average velocity of 4940 m/s, which indicates waves travelling in the metamorphic bedrock (Bælum et al., 2012). Assuming a P-wave velocity of 1700 m/s in the unconsolidated sediments (Plassen et al., 2004), simple geometric relations based on the known travel pattern of critically refracted seismic waves indicate an average sediment thickness of approximately 17 m here, suggesting that the glaciogenic sediments in Adolfbukta directly overlie the metamorphic basement.

CLASSIFICATION OF SEISMIC EVENTS

As the seismic receivers record all types of waves that reach their position, regardless of their source, we classify the recorded signals as (a) non-glacier-related events (earthquakes, airgun signals, boat traffic, ambient noise) and (b) glacier-related events.

Non-glacier-related events

Ambient noise due to wind and wave activity is constantly present in the data. During the study period, the weather conditions were relatively stable with air temperatures at the Pyramiden weather station remaining below 0°C and mean wind speeds remaining below 5 m/s, except for a 13-h period on 14 October when both temperature and mean wind speed were slightly higher (max. 2.1°C and 7.1 m/s, respectively) (The Norwegian Meteorological Institute (MET Norway), 2022). Temporal variations in the background noise level may lead to a varying threshold for which glacier-related events are detected. Additionally, previous studies in front of glaciers (e.g., Bartholomaus, Amundson, et al., 2015; Glowacki et al., 2016; Podolskiy et al., 2021) have recorded continuous seismic tremors due to subglacial discharge and basal sliding, processes which we do not consider in detail in this study. Noise from human activity, including boat and airgun noise, occurs in clearly defined time intervals and is therefore relatively easy to distinguish from icequakes.

TABLE 1   Characteristics of the main event groups.

Group	Dominant frequency range	Time domain signal characteristics	Suggested source mechanism
1	4–6 Hz	Emergent, multiple phase arrivals, 3–21 s duration (average: 7.7 s), followed by gravity waves	Calving into water
2	4–6 Hz	Emergent, multiple phase arrivals, 1–21 s duration (average: 4.4 s), weaker amplitude than group 1	Calving
3	>90 Hz	Impulsive, ≤1 s duration	Fracturing, crevassing
4	Multiple peaks, characteristic frequencies between 16 and 30 Hz	≤1 s duration	Resonance in water-filled cracks?

Note: See the 'Discussion' section for more details on the suggested source mechanisms.

Throughout the dataset, we observe events with clear P- and S-onsets, which are also clearly recorded at the permanent SPITS monitoring array (Schweitzer et al., 2021; waveform data retrieved from the European Integrated Data Archive, maintained by the University of Bergen and NORSAR) located at Janssonhaugen in Adventdalen about 53 km away. For these reasons, they are classified as earthquakes. These events typically have low dominant frequencies (8–9 Hz) and long duration (average: 35 s). In addition to this, several low SNR events with dominant frequencies of around 9–11 Hz and an average duration of 3 s are seen throughout the study period. Closer inspection of the direction and apparent velocity of these events shows that they originate from distant sources (either earthquakes or other glaciers) and are therefore not further investigated in this study.

Seismic signals from the glacier

The dataset includes numerous discrete seismic events which do not fit the descriptions above. These are signals of varying duration (0.1–21.0 s) originating from an eastern or northern direction that are assumed to be icequakes, generated by the glacier or nearby icebergs. We have manually picked events that were easily distinguishable from the ambient noise to be the focus of this study. However, more events are most definitely present in the data but are not emphasized due to their very low amplitude or short duration.

By displaying the manually picked events in the time and frequency domain, their signatures can be divided into four main groups, see Figure 4 and Table 1. Groups 1 and 2 (Figure 4a,b) represent emergent signals with similar frequency content, and a total of 144 of these events were picked. As opposed to earthquake events, they consist of multiple diffuse P- and S-phases which are difficult to distinguish. Group 1 events (30 events) are followed by low-velocity and long-period fluctuations,

which are gravity waves. Group 1 events generally have higher amplitudes and longer durations than group 2 events (114 events). We also observed Scholte waves subsequent to some events of both groups 1 and 2. Events in groups 3 and 4 are of shorter duration (≤1 s), but the two groups have contrasting frequency characteristics. Group 3 events (Figure 4c) are impulsive and narrow-band signals of varying amplitudes with significantly higher dominant frequencies (>90 Hz) than in the other groups. These events are frequently seen throughout the dataset, sometimes with several weak events occurring every minute. Finally, group 4 events (Figure 4d) consist of a main signal with energy distributed at peaks throughout the spectrum. Only three events of this type have been clearly identified in the dataset, and this group is as such only included as these events are very distinct and clearly have a different origin than the other events, and they also seem to originate from the direction of the glacier. Spectral peaks at integer multiples of the characteristic frequency (harmonics) suggest acoustic resonance. In this case, the frequency peaks are found close to (but not exactly) integer multiples, and not at the same frequencies for all events. Finally, Figure 4e shows an example of an earthquake for comparison.

Although the frequency content and duration of recorded seismic signals also depend on the travel path between source and receiver, the distinct differences between the groups suggest that various icequake source mechanisms are at play at Nordenskiöldbreen. Before we further discuss the possible source mechanisms suggested in Table 1, we review some characteristics of the identified gravity and Scholte waves.

Gravity waves

Figure 5a shows one event from group 1 followed by both gravity and Scholte waves within a record
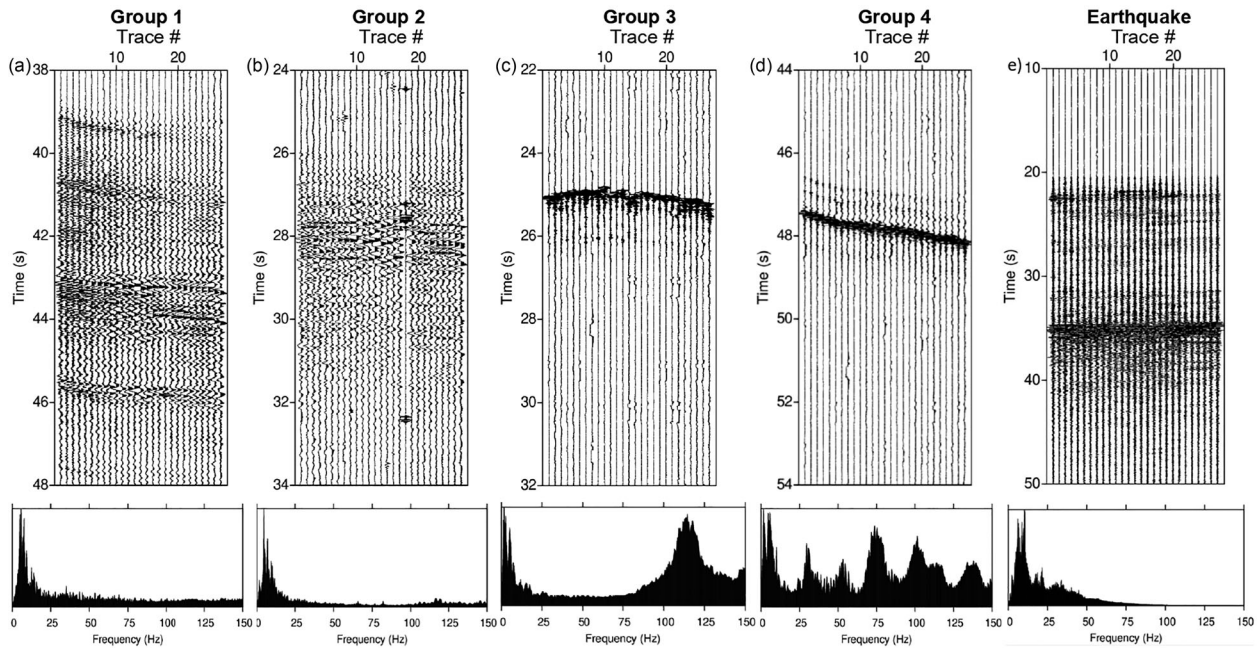
FIGURE 4 The various icequake events typically have characteristics that make them fit into one of the four groups listed in Table 1. The records show a representative event from each group, as well as a tectonic earthquake for comparison. Each record is 10 s long (except the longer earthquake record), bandpass-filtered between 1 and 150 Hz, and the averaged and normalized amplitude spectrum of each time window is shown below. The first two groups of events have similar amplitude spectra, suggesting a similar source mechanism. The third and fourth groups have different amplitude spectra and shorter duration. Traces are ordered from east to west, that is from closest to furthest from the glacier. (a) 12 October, 0513 UTC, peak at 4–6 Hz, followed by gravity waves; (b) 11 October, 1400 UTC, peak at 4–6 Hz (same event as in Figure 3); (c) 15 October, 0418 UTC, peak at >110 Hz (same event as in Figure 7b); (d) 15 October, 1424 UTC, many peaks; (e) 15 October, 1025 UTC, peak at 8–9 Hz.

length of 10 min. The event was recorded at the OBN hydrophone located closest to the glacier. The first arrivals, at about 07:47:45, combine a P-wave propagating in the water and an S-wave propagating below the seabed. A monochromatic Scholte wave arrives about 10 s later, before a long train of gravity waves with periods ranging from 10 to 30 s. This wave train is clearly dispersive where the long-periodic waves arrive first. Gravity waves are dispersive at water depths much larger than the wavelength and non-dispersive in shallow water (Reeve et al., 2012), and the water depths in Adolfbukta are between these extrema. Figure 5b shows low-pass filtered data in order to enhance the gravity waves. Finally, Figure 5c shows the corresponding wave heights at the water surface calculated using the conversion approach outlined in Appendix A. Note that estimated wave heights of less than 10 cm are much smaller than what we expect to be wind-generated in this area. The observation of distinct gravity waves in our OBN data therefore illustrates that the water layer acts as a low-pass filter, where wind-generated waves of relatively short wavelengths are dampened, whereas gravity waves of long wavelength from calving events are preserved. This demonstrates that hydrophones located at the seabed much better reveal calving events than hydrophones deployed at shallower depths.

Scholte waves

Hydrophones located at the seabed are also advantageous for recording Scholte waves, which are the only guided waves that may exist along the seabed in case the S-wave velocity of the seabed sediments is lower than the water P-wave velocity. This is likely the case for the loose glacial sediments in Adolfbukta, similar to nearby Sveabukta studied by Johansen and Ruud (2020). Scholte waves can be generated either by impact on the seabed itself or due to coupling with waves excited by a seismic source in the water close to the seabed. Figure 6a shows strong Scholte waves only on receivers closest to the glacier and, like gravity waves, only following some events. The former observation is probably due to the strong attenuation of Scholte waves as the distance from the source increases, and that the thickness of the seabed sediment layer decreases away from the glacier. We further hypothesize that Scholte waves are trailing only some events because they are generated when falling ice vertically impacts on the seabed, which may depend on calving volume, fall height and water depth. We assume this is a plausible explanation due to the shallow water depth in the area, but emphasize that also other processes during calving can impact the signal.
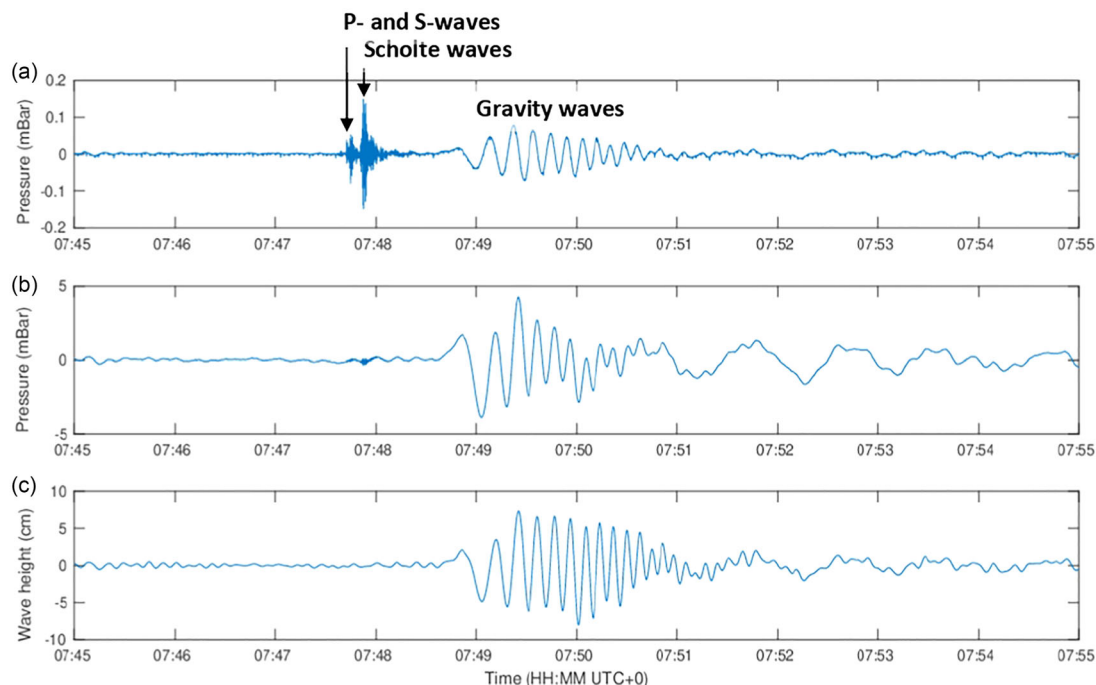
FIGURE 5 (a) A period of 10 min of hydrophone recording of an event on 12 October followed by Scholte and gravity waves. The ocean bottom node (OBN) was at 43 m water depth. The raw data have been converted to pressure and low-pass filtered with high-cut of 10 Hz. In (b), the recording has been processed by flattening the frequency response down to 0.01 Hz. Consequently, the amplitudes of the long period gravity waves have increased considerably (note the change in scale). There are also some very long periodic (about 1 min) monochromatic waves seen trailing the gravity waves, which are likely seiches (standing gravity waves). In (c), the data have been further compensated for the pressure reduction factor and converted to wave height at the surface. In order to remove the seismic waves (which would otherwise have been strongly magnified by the pressure compensation factor), the trace has been low-pass filtered below 0.15 Hz. The effect of the pressure compensation for this example is mainly to increase the amplitude of wave periods around 10 s. See Appendix A for more details.
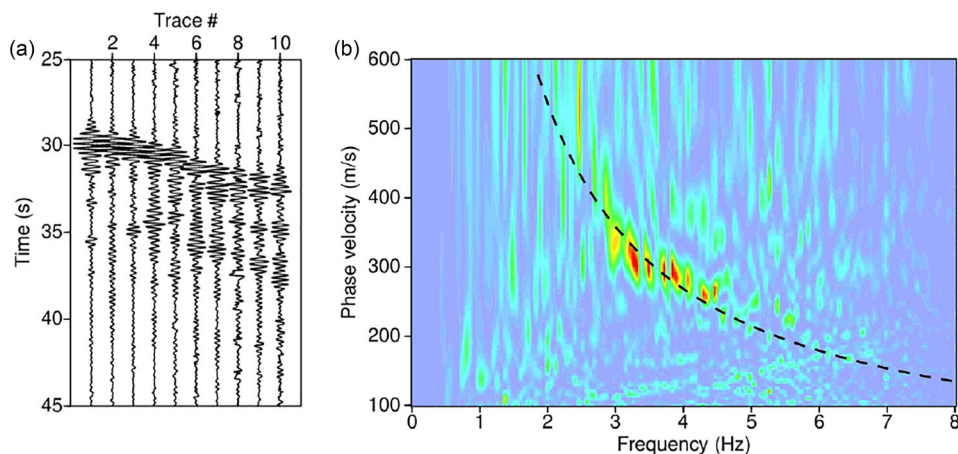
FIGURE 6 (a) Traces and (b) velocity spectrum of Scholte waves. The dashed curve shows the theoretical dispersion curve for the fundamental mode for $\nu = 0.5$ and $c_0 = 76$ m/s, which fits relatively well with the spectral peaks in the dispersion image in the 2.5–5 Hz frequency range. We here assume that the sediment density is 1.5 times the water density and use $\nu = 0.5$ for simplicity.

Plots of phase velocity versus frequency (dispersion images) (Figure 6b) generated based on the method outlined in Park et al. (1998) show that Scholte waves have their main energy within a frequency band of 2.5–5 Hz. The various frequency components of the Scholte wave

are affected by different seabed layers. Previous studies (e.g., Boiero et al., 2013; Johansen & Ruud, 2020) show how dispersion analysis can reveal the mechanical properties of the near-surface sediments through inversion for S-wave velocity profile. In areas with active

sedimentation of fine particles, the seabed is occurring as a suspension with almost no shear strength. In such cases, a simpler approach of using a power-law equation may be sufficient to approximate the upper S-wave velocity profile (Chapman & Godin, 2001):

$$V_S = c_0 \, z^{\nu}, \tag{1}$$

where z is the depth below seafloor, c_0 is the velocity at unit depth ($z = 1$ m) and the exponent ν is typically in the interval 0.2–0.8 (Chapman & Godin, 2001; Hamilton, 1976; Williams et al., 2021). For $\nu = 0.5$, Godin and Chapman (2001) and Chapman and Godin (2001) showed that the phase and group velocities of Scholte waves (both fundamental and higher modes) are given by very simple formulas. The phase velocity of the fundamental mode is then (Chapman & Godin, 2001)

$$V_0 = c_0^2 \, / \pi f \, (1 + R), \tag{2}$$

where f is the frequency, and R is the ratio between the densities of water and sediment. When ν deviates from 0.5, approximate formulas exist (Chapman & Godin, 2001). By curve-fitting with the dispersion spectrum peaks in the relevant frequency range and applying Equations (1) and (2), we can approximate the depth-dependent S-wave velocity of the shallow sediments in Adolfbukta by $V_S = 76\sqrt{z}$ m/s, corresponding to the dashed curve in Figure 6b. This low velocity implies that the seabed sediments in Adolfbukta are very soft.

LOCALIZATION OF GLACIAL EVENTS

A motivation for using several receivers in seismic campaigns is that this enhances the possibility of event localization which can thereby reveal the source mechanism. For example, while calving occurs only at the glacier terminus, fracturing and crevassing may happen within the glacier or in floating icebergs.

However, source localization of calving events is not straightforward as these seismic events are emergent and with a relatively long duration (>1 s). This is because even small calving events typically last for more than a second and are often instantaneously followed by additional small calving events. Hence, it is impossible to pick accurate onset times of the different phases which overlap in time. In the rare cases of impulsive onsets, it is possible to locate events close to the array based on first arrivals only, but the location uncertainty (in particular, the distance to the event) increases rapidly with offset. Onset times of secondary phases could have resolved the distance based on differential travel times (i.e., the time difference between P- and S-phases), but this is also hampered by the emergent onsets and overlapping phases. Similar difficulties

in source localization are described by Vinogradov et al. (2016) who used a small joint seismic-infrasound array situated in Pyramiden to monitor icequakes from Nordenskiöldbreen.

Broadband *fk*-analysis can give more accurate estimates of the azimuth and apparent velocity of the waves, but again, overlapping phases and multipathing in the water layer make the waves from calving events incoherent and unsuitable for such analysis. As the OBNs also record a lot of high-frequency noise, which seems uncorrelated across the receivers, attempts at source localization using matched field processing (similar to Romeyn et al., 2021) fail. For distant events, like earthquakes, the wavefield appears much more coherent over the OBN array and *fk*-analysis works well. An alternative method for array analysis of events with incoherent wavefields is to use envelope traces (i.e., 'incoherent beamforming'), but the resolution of such methods is low and only provides the direction (azimuth) towards the event, which we can also obtain visually from the recordings. For example, from the traces in Figure 4, it is obvious from the event slopes that the events in (a) and (d) propagated in direction from east towards west, that is from the southern glacier terminus towards the OBN array, whereas in (b), the waves propagated more normal to the array, that is from the northern part of the glacier terminus. Overall, the clear majority of calving events originate from the southern margin of the glacier, consistent with previous studies (Allaart et al., 2018), whereas fracturing events originate both from the glacier and from floating icebergs.

The geophones on land record air waves in addition to P- and S-waves. For calving events with a relatively simple source function, such as in Figure 7a, we can determine the travel time difference between the P- and the air wave and then estimate the distance to the event. As the wavefields are rather incoherent also between land nodes, we cannot find accurate azimuths by ordinary array processing, but if we assume that the calving events occur along the glacier terminus, we can approximate the event location using the distance only as demonstrated in Figure 7c. The event in Figure 7b is an example of an event with an impulsive onset and short distance and thus can be located by a least-square inversion method using first onsets only.

DISCUSSION

In our study, we deployed a large number of hydrophones and geophones in the immediate vicinity of the glacier, both on land and at the seabed. Köhler et al. (2019) compared measurements immediately in front of a glacier with a permanent seismic station in Ny-Ålesund 15 km away and found that 10%–45% of the calving events could also be detected at the permanent
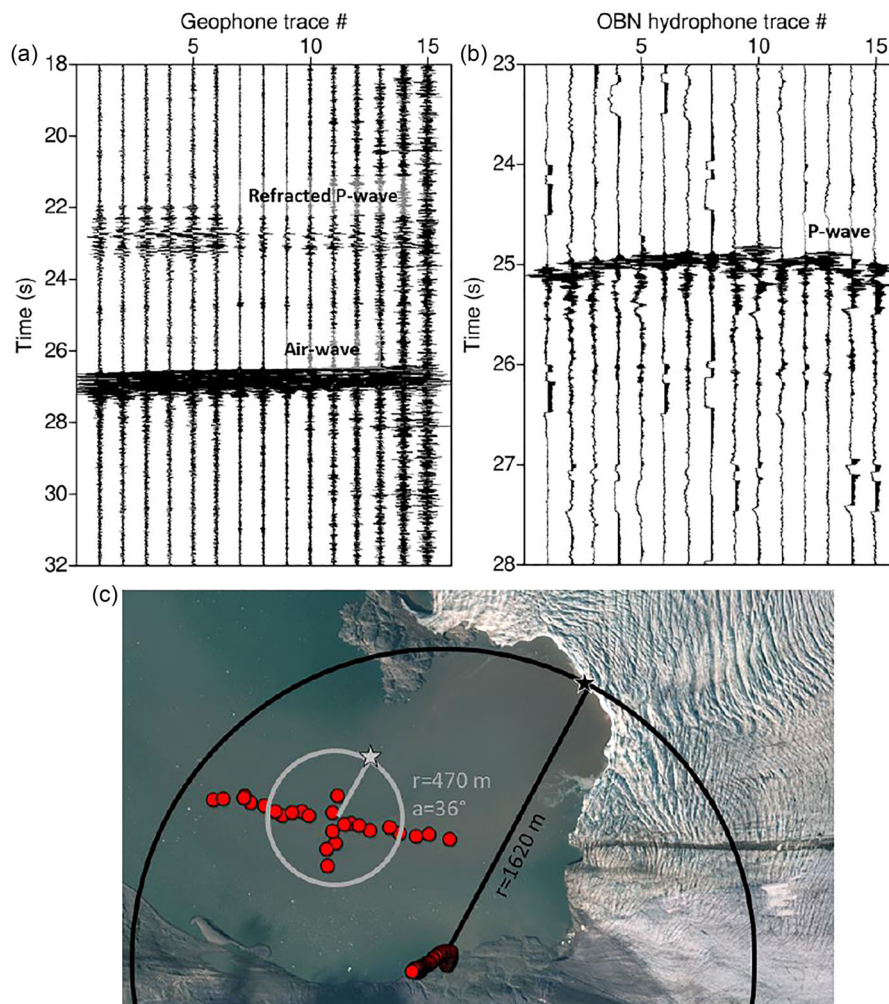
FIGURE 7   (a) A group 1 calving event recorded at the land geophones of the south array on 12 October. We observe two distinct phases: a refracted (direct) P-wave arrival at 22.0 s, and a stronger air wave arrival at 26.6 s. (b) A group 3 cracking event recorded at the ocean bottom node (OBN) hydrophones on 15 October. Note the shorter time axis than in (a). We only observe one clear phase, arriving at different times at the different hydrophones. (c) From the time difference between the arrivals and assuming a P-wave velocity of 5000 m/s and an air wave velocity of 330 m/s, we find that the event in (a) was located 1620 m away from the south array geophones. Hence, we estimate the calving location to be at the cross-point between the black circle (r = 1620 m) and the glacier terminus (black star). For the event in (b), least-squares fitting of observed and computed travel times for an assumed water velocity of 1455 m/s yields a source distance of 470 m (grey circle) and azimuth of 36° from the centre of the OBN array. The estimated source location is marked by the grey star, that is the event occurred in a floating iceberg.

station. Here, we cannot identify any of our recorded events at the permanent SPITS array, which may be due to the relatively large distance to the array and the comparatively small calving events at Nordenskiöldbreen. This demonstrates the advantage of having seismic receivers close to the glacier.

We show that seismic signals from the glacier cover the entire sampled frequency range from <1 Hz to 250 Hz, indicating the advantage of using a short sampling interval (2 ms) in comparison with other studies analysing events from various icequake sources. Although previous studies mostly rely on geophone data supplemented by one or a few hydrophones, our study emphasizes that a suite of events is easier to distinguish on hydrophones than on geophones due to an overall lower noise level in the relevant frequency range (Figure 3). Deploying hydrophones at the seabed rather than at shallow depths eases the detection of gravity and Scholte waves. Although the OBNs were designed for use in seismic exploration, the gentle slope of the hydrophone low-cut filter implies that they can also record signals of much lower frequencies (lower than geophones which always have a slope of 12 dB/octave below their natural frequency), as demonstrated here by the clear detection of gravity waves. The quality of the geophones onshore would be better by burying the receivers, but this is not permitted in this area.

Possible source mechanisms

The strongest transient seismic signals generated by the glacier are emergent, with dominant frequencies of around 4–6 Hz and durations of 1–21 s (groups 1–2). This corresponds well with signals of calving events reported in previous studies, although the dominant frequencies are slightly higher than in most studies (1–5 Hz) (Podolskiy & Walter, 2016). We explain this by less attenuation in this study compared with other studies due to the short distance from source to receiver, and the frequency response of our receivers which may not properly detect the lowermost frequencies. Calving as the source of these signals is also supported by the observation of gravity and Scholte waves following some signals.

The varying duration of calving events is probably linked to calving size, as previous studies have linked icequake duration and calving volume, although a simple relation does not seem to exist (O'Neel et al., 2007; Qamar, 1988; Bartholomaus, Larsen et al., 2015). Further, we cannot exclude the possibility that some events in groups 1 and 2 are due to basal stick–slip motion or submarine events, which both can occur in a similar frequency range as subaerial calving events, but with weaker amplitudes (Köhler et al., 2019; Podolskiy & Walter, 2016). However, submarine calving is generally less common than subaerial calving at marine-terminating glaciers (Glowacki, 2022) and is probably particularly rare here as the water depth at the glacier front is shallow. Geophones were not possible to safely deploy on Nordenskiöldbreen due to crevassing and polar bears frequenting the area. Polarization analysis of such data would improve localization and classification of icequakes from fracturing and basal motion because shear slip leads to dilatational first arrivals up-glacier and compressional first arrivals down-glacier from the event (Walter et al., 2008).

The short duration, narrow-frequency-band and impulsive nature of group 3 events correlate with previously described signals of brittle fracturing, either within the glacier, in the crevassing zone, or in floating ice (Podolskiy & Walter, 2016). Deichmann et al. (2000) showed that near-surface crevassing can be distinguished from deeper fracturing based on the presence of strong Rayleigh wave arrivals rather than dominant impulsive P- and S-wave arrivals in land geophone records. In practice, this means that as the Rayleigh phase is of lower frequency than the P- and S-phases, the dominant frequency can be used for discrimination between shallow and deep icequakes. For example, Röösli et al. (2014) observed near-surface crevassing events with dominant frequencies of 10–50 Hz and deep icequakes with dominant frequencies of 80–200 Hz. However, this distinction is only relevant for icequakes at depths larger than the Rayleigh wavelength (approx-imately 40–60 m in previous studies; Deichmann et al, 2000; Stuart et al., 2005). We observe a vast number of events with dominant frequencies varying between 90 Hz and 220 Hz and varying amplitudes, and at similar frequencies on both hydrophones and geophones, suggesting that they represent fracturing in different locations and of varying magnitudes. We further observe events both where the waves arrive first at OBNs closest to the glacier (trace 1), and where they arrive first at OBNs in the middle of the array (e.g., trace 7 or trace 21), suggesting that we recorded fracturing both in the glacier and in floating ice.

Group 4 is by far the smallest group, and only a few events of this type have been identified. Due to the scarcity and variation of these events, we cannot draw a definite conclusion about their source mechanism, but they seem to originate from the southern margin of the glacier. Acoustic resonance has previously been observed in many geologic systems (including glaciers) due to resonant vibrations of hydraulic fractures (Lipovsky & Dunham, 2015). The amplitude spectra somewhat resemble those observed and attributed to resonance in a fluid-filled crack by Stuart et al. (2005) at the surging Bakaninbreen glacier in Svalbard, although covering a broader frequency range here. We therefore propose that these events may be due to a similar mechanism, but resonance in the water layer may also be the source of these events.

Temporal variations

The limited duration of our acquisition implies that the data records are too short to reliably correlate the timing of events with tide phases and weather conditions. Calving at Svalbard tidewater glaciers typically peaks in August and September (Köhler et al., 2015). We observe no pattern in the occurrence frequency of calving events throughout the study period, although previous studies (e.g., Bartholomaus, Larsen, et al., 2015; Minowa et al., 2019; O'Neel et al., 2003) have correlated variations in calving rate with both air temperature and effective pressure variation at the terminus, and Köhler et al. (2019) recorded fewer calving signals on days with more ambient noise due to rougher weather conditions.

We record a decreasing number of gravity waves further out in the study period (correlating with increasing tide variations) and observe a tendency of more gravity waves occurring at high tide than at low tide. Minowa et al. (2019), on the other side, recorded more gravity waves during falling and low tide. A possible explanation for our observation is that more ice falls into the water as opposed to onto the ground at high tide at this mixed-terminus glacier, but longer data records are needed to confirm this observation. Further, we record less gravity waves on the day with the strongest winds (14 October).

Stronger waves due to rougher weather may disturb the water pressure to larger depths, possibly reaching the seabed receivers and thus preventing the detection of gravity waves.

Limitations and future improvements

A limitation of our study compared with previous studies (e.g., Bartholomaus et al., 2012; Köhler et al., 2019) is that, except for a few visual observations that correlate well with our data analysis (e.g., a calving event that was observed during deployment of equipment correlates with a detected group 1 event), we have no visual records of when calving occurred and thus cannot validate that the events are correctly classified. Poor visibility, cold air temperatures leading to rapid battery degradation and few daylight hours in October were the main reasons why no such monitoring was included in this study. However, the presence of gravity waves and Scholte waves following some events strongly indicates that these events are calving events (although gravity waves may in principle also be generated due to the break-up or capsizing of preexisting icebergs; Minowa et al., 2019), warranting the assumption that events with similar characteristics are also related to calving. For fracturing events, it is unlikely that these could have been observed, although large crevasses may be visible in satellite images (Winberry et al., 2020). Nevertheless, the limited temporal sampling of satellite images makes it difficult to associate near-surface crevassing with specific seismic events.

Several recent studies (e.g., Bartholomaus, Larsen, et al., 2015; Köhler et al., 2019; Sergeant et al., 2019) have attempted to extend the use of passive seismic monitoring in glacier environments from simply detection of icequakes to quantification of calving rates and volumes. These studies demonstrate that the relation between seismic signal characteristics and calving volume is strongly empirical, and that developing a universally applicable model to estimate calving volume from such signals is difficult. On another side, Minowa et al. (2019) estimated the calving rate of a marine-terminating glacier in Greenland using the amplitude and occurrence frequency of gravity waves. In our case, a particular problem is that Nordenskiöldbreen is partly terrestrial- and partly tidewater-terminating. Bartholomaus et al. (2012) noted that the ice–sea surface interaction rather than the actual rupture process itself was the main source of large icequake amplitudes and that different seismic events were recorded when ice fell into crevasses rather than into water. Hence, developing a model applicable to Nordenskiöldbreen is likely impossible without considering the calving location along the terminus and timing relative to tide phases.

We suggest that future studies on similar datasets focus on accurate source localization to better constrain the various source mechanisms. The data acquisition should also be of longer duration (ideally permanent) and include visual monitoring (e.g., time-lapse photography) to better understand the temporal variation in event occurrence.

CONCLUSIONS

A seismic field campaign was conducted in front of Nordenskiöldbreen on Svalbard in October 2020 using a variety of seismic receivers in water and on land. In this study, we analysed the acquired passive seismic data with respect to various types of seismic events and data quality. Our interpretations include events generated by glacier calving, fracturing/crevassing in the glacier and floating ice and possibly resonance in fluid-filled cracks, demonstrating the potential of using seismic in future monitoring of glacier dynamics. We also detect strong gravity and Scholte waves on seabed receivers, emphasizing that hydrophones at the seabed record gravity waves with a strong SNR. Scholte waves generated by the glacier can be used to unveil information about the strength of the seabed sediments. The most important outcome of this case study is the advance in knowledge about ideal survey design for seismic glacier monitoring, in particular, the benefit of including seabed receivers.

CONFLICT OF INTEREST STATEMENT
The authors declare that no conflicts of interest exist for all authors.

DATA AVAILABILITY STATEMENT
The data that support the findings of this study are available from the corresponding author upon reasonable request.

ORCID
Helene Meling Stemland https://orcid.org/0000-0002-0878-0473

Bent Ole Ruud https://orcid.org/0000-0002-6813-9215

Tor Arne Johansen https://orcid.org/0000-0002-3974-1362

REFERENCES

Allaart, L., Friis, N., Ingólfsson, Ó., Håkansson, L., Noormets, R., Farnsworth, W.R. et al. (2018) Drumlins in the Nordenskiöldbreen forefield, Svalbard. *GFF*, 140(2), 170–188. https://doi.org/10.1080/11035897.2018.1466832

Bartholomaus, T.C., Larsen, C.F., O'Neel, S. & West, M.E. (2012) Calving seismicity from iceberg–sea surface interactions. *Journal of Geophysical Research: Earth Surface*, 117(F4), F04029. https://doi.org/10.1029/2012JF002513

Bartholomaus, T.C., Amundson, J.M., Walter, J.I., O'Neel, S., West, M.E. & Larsen, C.F. (2015) Subglacial discharge at tidewater glaciers revealed by seismic tremor. *Geophysical Research Letters*, 42(15), 6391–6398. https://doi.org/10.1002/2015GL064590

Bartholomaus, T.C., Larsen, C.F., West, M.E., O'Neel, S., Pettit, E.C. & Truffer, M. (2015) Tidal and seasonal variations in calving flux observed with passive seismology. *Journal of Geophysical Research: Earth Surface*, 120(11), 2318–2337.

Blinova, M., Faleide, J.I., Gabrielsen, R.H. & Mjelde, R. (2013) Analysis of structural trends of sub-sea-floor strata in the Isfjorden area of the West Spitsbergen Fold-and-Thrust Belt based on multichannel seismic data. *Journal of the Geological Society*, 170(4), 657–668. https://doi.org/10.1144/jgs2012-109

Boiero, D., Wiarda, E. & Vermeer, P. (2013) Surface-and guided-wave inversion for near-surface modeling in land and shallow marine seismic data. *The Leading Edge*, 32(6), 638–646. https://doi.org/10.1190/tle32060638.1

Bælum, K., Johansen, T.A., Johnsen, H., Rød, K., Ruud, B.O. & Braathen, A. (2012) Subsurface structures of the Longyearbyen CO_2 Lab study area in Central Spitsbergen (Arctic Norway), as mapped by reflection seismic data. *Norwegian Journal of Geology*, 92(4), 377–389.

Chapman, D.M.F. & Godin, O.A. (2001) Dispersion of interface waves in sediments with power-law shear speed profiles. II. Experimental observations and seismo-acoustic inversions. *Journal of the Acoustical Society of America*, 110(4), 1908–1916. https://doi.org/10.1121/1.1401739

Crameri, F. (2018) Scientific colour-maps. *Zenodo*, 10, https://doi.org/10.5281/zenodo.1243862

Deichmann, N., Ansorge, J., Scherbaum, F., Aschwanden, A., Bernard, F. & Gudmundsson, G.H. (2000) Evidence for deep icequakes in an Alpine glacier. *Annals of Glaciology*, 31, 85–90. https://doi.org/10.3189/172756400781820462

Den Ouden, M.A.G., Reijmer, C.H., Pohjola, V., Van De Wal, R.S.W., Oerlemans, J. & Boot, W. (2010) Stand-alone single-frequency GPS ice velocity observations on Nordenskiöldbreen, Svalbard. *The Cryosphere*, 4(4), 593–604. https://doi.org/10.5194/tc-4-593-2010

Elvevold, S., Dallmann, W. & Blomeier, D. (2007) *Geology of Svalbard*. Tromsø: Norwegian Polar Institute.

Ewertowski, M.W., Evans, D.J., Roberts, D.H. & Tomczyk, A.M. (2016) Glacial geomorphology of the terrestrial margins of the tidewater glacier, Nordenskiöldbreen, Svalbard. *Journal of Maps*, 12(Supplement 1), 476–487. https://doi.org/10.1080/17445647.2016.1192329

Farnsworth, W.R., Ingólfsson, Ó., Retelle, M. & Schomacker, A. (2016) Over 400 previously undocumented Svalbard surge-type glaciers identified. *Geomorphology*, 264, 52–60. https://doi.org/10.1016/j.geomorph.2016.03.025

Godin, O.A. & Chapman, D.M.F. (2001) Dispersion of interface waves in sediments with power-law shear speed profiles: I. Exact and approximate analytical results. *Journal of the Acoustical Society of America*, 110(4), 1890–1907. https://doi.org/10.1121/1.1401776

Glowacki, O. (2022) Distinguishing subaerial and submarine calving with underwater noise. *Journal of Glaciology*, 68(272), 1185–1196. https://doi.org/10.1017/jog.2022.32

Glowacki, O., Moskalik, M. & Deane, G.B. (2016) The impact of glacier meltwater on the underwater noise field in a glacial bay. *Journal of Geophysical Research: Oceans*, 121(12), 8455–8470. https://doi.org/10.1002/2016JC012355

Hamilton, E.L. (1976) Shear-wave velocity versus depth in marine sediments: a review. *Geophysics*, 41(5), 985–996. https://doi.org/10.1190/1.1440676

Hudson, T.S., Brisbourne, A.M., Walter, F., Gräff, D., White, R.S. & Smith, A.M. (2020) Icequake source mechanisms for studying glacial sliding. *Journal of Geophysical Research: Earth Surface*, 125(11), e2020JF005627. https://doi.org/10.1029/2020JF005627

Johansen, T.A. & Ruud, B.O. (2020) Characterization of seabed properties from Scholte waves acquired on floating ice on shallow water. *Near Surface Geophysics*, 18(1), 49–59. https://doi.org/10.1002/nsg.12082

Köhler, A., Nuth, C., Schweitzer, J., Weidle, C. & Gibbons, S.J. (2015) Regional passive seismic monitoring reveals dynamic glacier activity on Spitsbergen, Svalbard. *Polar Research*, 34(1), 26178. https://doi.org/10.3402/polar.v34.26178

Köhler, A., Pętlicki, M., Lefeuvre, P.M., Buscaino, G., Nuth, C. & Weidle, C. (2019) Contribution of calving to frontal ablation quantified from seismic and hydroacoustic observations calibrated with lidar volume measurements. *The Cryosphere*, 13(11), 3117–3137. https://doi.org/10.5194/tc-13-3117-2019

Lipovsky, B.P. & Dunham, E.M. (2015) Vibrational modes of hydraulic fractures: Inference of fracture geometry from resonant frequencies and attenuation. *Journal of Geophysical Research: Solid Earth*, 120(2), 1080–1107. https://doi.org/10.1002/2014JB011286

Meier, M.F., Dyurgerov, M.B., Rick, U.K., O'Neel, S., Pfeffer, W.T., Anderson, R.S. et al. (2007) Glaciers dominate eustatic sea-level rise in the 21st century. *Science*, 317(5841), 1064–1067. https://doi.org/10.1126/science.1143906

Meredith, M., Sommerkorn, M., Cassotta, S., Derksen, C., Ekaykin, A., Hollowed, A., Kofinas, G., Mackintosh, A., Melbourne-Thomas, J., Muelbert, M.M.C., Ottersen, G., Pritchard, H., & Schuur, E.A.G. (2019) Polar regions. In: Pörtner, H.-O., Roberts, D.C., Masson-Delmotte, V., Zhai, P., Tignor, M., Poloczanska, E., Mintenbeck, K., Alegría, A., Nicolai, M., Okem, A., Petzold, J., Rama, B., Weyer, N.M. (Eds.) *IPCC special report on the ocean and cryosphere in a changing climate*. Cambridge, UK and New York, NY, USA: Cambridge University Press, pp. 203–320. https://doi.org/10.1017/9781009157964.005

Minowa, M., Podolskiy, E.A., Jouvet, G., Weidmann, Y., Sakakibara, D., Tsutaki, S. et al. (2019) Calving flux estimation from tsunami waves. *Earth and Planetary Science Letters*, 515, 283–290. https://doi.org/10.1016/j.epsl.2019.03.023

Neave, K.G. & Savage, J.C. (1970) Icequakes on the Athabasca glacier. *Journal of Geophysical Research*, 75(8), 1351–1362. https://doi.org/10.1029/JB075i008p01351

O'Neel, S., Echelmeyer, K.A. & Motyka, R.J. (2003) Short-term variations in calving of a tidewater glacier: LeConte Glacier, Alaska, USA. *Journal of Glaciology*, 49, (167), 587–598. https://doi.org/10.3189/172756503781830430

O'Neel, S., Marshall, H.P., McNamara, D.E. & Pfeffer, W.T. (2007) Seismic detection and analysis of icequakes at Columbia Glacier, Alaska. *Journal of Geophysical Research: Earth Surface*, 112(F3), F03S23. https://doi.org/10.1029/2006JF000595

Park, C.B., Miller, R.D. & Xia, J. (1998) Imaging dispersion curves of surface waves on multi-channel record. In: SEG *Technical Program Expanded Abstra*cts 1998. Houston, Society of Exploration Geophysicists. pp. 1377–1380.

Plassen, L., Vorren, T.O. & Forwick, M. (2004) Integrated acoustic and coring investigation of glacigenic deposits in Spitsbergen fjords. *Polar Research*, 23(1), 89–110. https://doi.org/10.1111/j.1751-8369.2004.tb00132.x

Podolskiy, E.A. & Walter, F. (2016) Cryoseismology. *Reviews of geophysics*, 54(4), 708–758. https://doi.org/10.1002/2016RG000526

Podolskiy, E.A., Murai, Y., Kanna, N. & Sugiyama, S. (2021) Ocean-bottom and surface seismometers reveal continuous glacial tremor and slip. *Nature Communications*, 12(1), 1–11. https://doi.org/10.1038/s41467-021-24142-4

Qamar, A. (1988) Calving icebergs: a source of low-frequency seismic signals from Columbia Glacier, Alaska. *Journal of Geophysical Research: Solid Earth*, 93(B6), 6615–6623. https://doi.org/10.1029/JB093iB06p06615

Reeve, D., Chadwick, A. & Fleming, C. (2012) *Coastal engineering: processes, theory and design practice*, 2nd edition, London: Spon Press.

Romeyn, R., Hanssen, A., Ruud, B.O., Stemland, H.M. & Johansen, T.A. (2021) Passive seismic recording of cryoseisms in Adventdalen, Svalbard. *The Cryosphere*, 15(1), 283–302. https://doi.org/10.5194/tc-15-283-2021

Röösli, C., Walter, F., Husen, S., Andrews, L.C., Lüthi, M.P., Catania, G.A. et al. (2014) Sustained seismic tremors and icequakes detected in the ablation zone of the Greenland ice sheet. *Journal of Glaciology*, 60(221), 563–575. https://doi.org/10.3189/2014JoG13J210

Schweitzer, J., Köhler, A. & Christensen, J.M. (2021) Development of the NORSAR Network over the Last 50 Yr. *Seismological Research Letters*, 92(3), 1501–1511. https://doi.org/10.1785/0220200375

Sergeant, A., Mangeney, A., Yastrebov, V.A., Walter, F., Montagner, J.P., Castelnau, O. et al. (2019) Monitoring Greenland ice sheet buoyancy-driven calving discharge using glacial earthquakes. *Annals of Glaciology*, 60(79), 75–95. https://doi.org/10.1017/aog.2019.7

Stemland, H.M., Johansen, T.A., Ruud, B.O. & Aniceto, A.S. (2019) Measured sound levels in ice-covered shallow water caused by seismic shooting on top of and below floating ice, reviewed for possible impacts on true seals. *First Break*, 37(1), 35–42. https://doi.org/10.3997/1365-2397.2018010

Stuart, G., Murray, T., Brisbourne, A., Styles, P. & Toon, S. (2005) Seismic emissions from a surging glacier: Bakaninbreen, Svalbard. *Annals of Glaciology*, 42, 151–157. https://doi.org/10.3189/172756405781812538

Trupp, R., Hastings, J., Cheadle, S. & Vesely, R. (2009) Seismic in arctic environs: meeting the challenge. *The Leading Edge*, 28(8), 936–942. https://doi.org/10.1190/1.3192840

Van Pelt, W.J.J., Oerlemans, J., Reijmer, C.H., Pohjola, V.A., Pettersson, R. & Van Angelen, J.H. (2012) Simulating melt, runoff and refreezing on Nordenskiöldbreen, Svalbard, using a coupled snow and energy balance model. *The Cryosphere*, 6(3), 641–659. https://doi.org/10.5194/tc-6-641-2012

Vinogradov, A., Asming, V., Baranov, S., Fedorov, A. & Vinogradov, Y. (2016) Joint seismo-infrasound monitoring of outlet glaciers in the Arctic: case study of the Nordenskiold outlet glacier terminus near Pyramiden (Spitsbergen). In: 16th International Multidisciplinary Scientific GeoConference SGEM, *Sofia, Bulgaria*, vol. 3. SGEM. p. 521.

Walter, F., Deichmann, N. & Funk, M. (2008) Basal icequakes during changing subglacial water pressures beneath Gornergletscher, Switzerland. *Journal of Glaciology*, 54(186), 511–521. https://doi.org/10.3189/002214308785837110

Williams, E.F., Fernández-Ruiz, M.R., Magalhaes, R., Vanthillo, R., Zhan, Z., González-Herráez, M. et al. (2021) Scholte wave inversion and passive source imaging with ocean-bottom DAS. *The Leading Edge*, 8, 576–583. https://doi.org/10.1190/tle40080576.1

Winberry, J.P., Huerta, A.D., Anandakrishnan, S., Aster, R.C., Nyblade, A.A. & Wiens, D.A. (2020) Glacial earthquakes and precursory seismicity associated with Thwaites Glacier calving. *Geophysical Research Letters*, 47(3), e2019GL086178. https://doi.org/10.1029/2019GL086178

A | GRAVITY WAVES

Dispersion of gravity waves

The surface elevation η of a gravity wave with constant wavelength L and period T, propagating with increasing distance x and time t, may be written as (Reeve et al., 2012)

$$\eta = \frac{H}{2} \cos \left\{ 2\pi \left(\frac{x}{L} - \frac{t}{T} \right) \right\} = \frac{H}{2} \cos (kx - \omega t),$$
(A1)

where H is the wave height (measured from through to peak), $k = \frac{2\pi}{L}$ is the angular wavenumber, and $\omega = \frac{2\pi}{T} = 2\pi f$ is the angular frequency.

The propagation velocity $c = \frac{L}{T} = \frac{\omega}{k}$ of the wave depends on the water depth D and can be found by solving the dispersion equation (Reeve et al., 2012):

$$\omega^2 = gk \ \tanh(kD),$$
(A2)

where g is the gravitational acceleration. Due to the multiple unknown variables, Equation (A2) generally must be solved numerically, except in some special cases:

- When the wavelength is much larger than the water depth ($L > 20D$), we have $\tanh(kD) \approx kD$; hence, the waves are non-dispersive with velocity $c = \sqrt{gD}$.
- For wavelengths less than about two times the water depth, we have $\tanh(kD) \approx 1$, which gives dispersive waves with velocity $c = \frac{g}{\omega}$.

In our case, the wavelength and water depth are so that neither of these special cases applies, and the dispersion equation must be solved numerically. Figure A1 shows how the wavelength and phase velocity vary for the water depths and periods that apply to our observations of gravity waves generated by calving events.

Further, the pressure P at depth z (measured downward from the still water level) under the gravity wave is given by (Reeve et al., 2012)

$$P(z) = \rho gz + \rho g\eta \ K_\rho(z),$$
(A3)
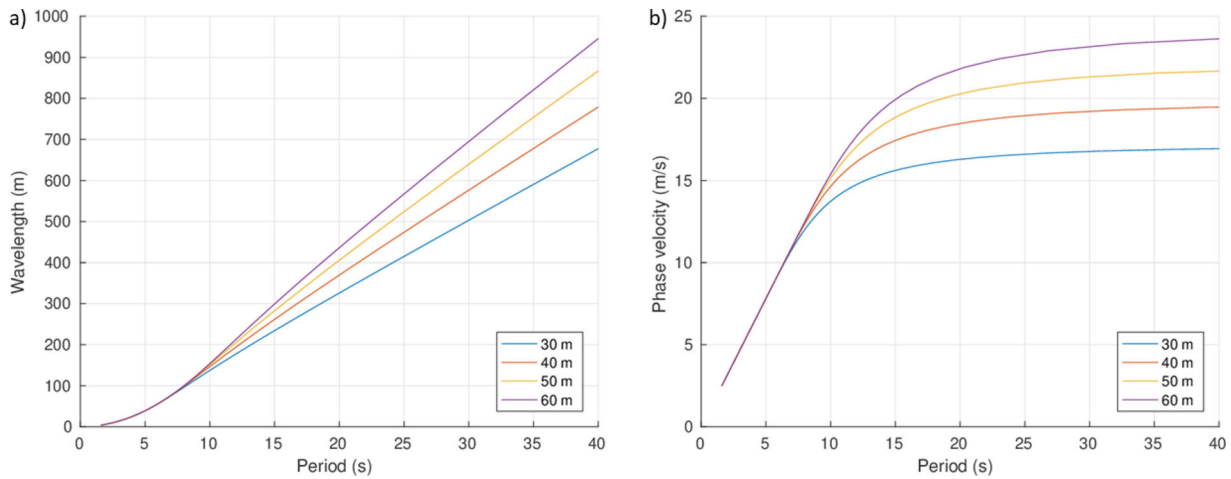
FIGURE A1 (a) The wavelength of gravity waves computed from the dispersion Equation (A2) for various wave periods and water depths in the range 30–60 m. (b) The phase velocity of gravity waves computed for various wave periods and water depths.

where ρ is the water density and K_p, the pressure attenuation factor, is given by

$$K_p(z) = \frac{\cosh\{k(D-z)\}}{\cosh(kD)}. \tag{A4}$$

From Equation (A3), we see that the pressure is the sum of a static term due to the water depth and a time-varying term due to the gravity wave (Equation A1).

A hydrophone record will only reveal the time-varying term as the instrument is insensitive to static pressure. The pressure variations due to the gravity wave are attenuated depending on the wavelength and water depth. At the seabed, the pressure attenuation factor reduces to

$$K_p(z = D) = (\cosh(kD))^{-1}. \tag{A5}$$

For water depths much less than the wavelength, K_p is close to unity, whereas it decays fast with increasing depth. Figure A2 shows how the pressure attenuation factor for a sensor at the seabed varies with various water depths and wave periods. In practice, the water layer acts as a low-pass filter, removing short wind-generated waves and passing long gravity waves generated by calving events. Hence, this demonstrates the advantage of using receivers at the seabed compared with higher up in the water column to record gravity waves.

Conversion of hydrophone recording to wave height
In Figure 5, the hydrophone recording (Figure 5a) was first Fourier transformed into the frequency domain, where a correction for the known frequency response of the hydrophone was applied. This correction affects both the amplitude and phase of the recording. A transform back to time domain gave the trace shown in Figure 5b.
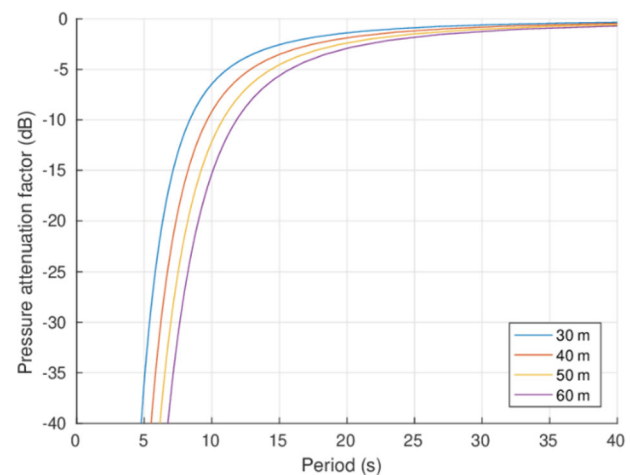
FIGURE A2 The pressure attenuation factor for a sensor at the seafloor computed for various wave periods and water depths. Note that when the water depth is half the wavelength, the attenuation is more than 20 dB.

To correct for the pressure reduction factor, the dispersion relation (Equation A2) was used to convert between frequency and the wavenumber in Equation (A5) for the given depth of the node. As the pressure reduction factor is a real number, this correction was applied only to the amplitude of the Fourier transformed recording. An inverse Fourier transform back to time domain gave the result shown in Figure 5c.

Although the wave height in Figure 5c is only about 16 cm (from trough to peak), the actual wave height when the wave hits the shore is considerably larger. When a wave approaches the shore, its velocity (and wavelength) will decrease with the square root of depth, and for the wave to preserve its energy, the amplitude must increase. Eventually, the wave will become so steep that it breaks. Exactly when this occurs is

difficult to predict, but a conservative estimate is that the wave height increases by approximately 300% relative to the wave height estimated at the node before the wave breaks at the shore. As an example, a different calving event which happened late on 15 October (close to spring tide) had wave amplitudes nearly twice that of the event in Figure 5 and was probably responsible for flooding several of our land geophones.